Equilibrium shapes of two and three dimensional two-phase rotating fluid drops with surface tension: effects of inner drop displacement

S. L. Butler[1]

Department of Geological Sciences, University of Saskatchewan, Saskatoon, SK, S7N 5E2, Canada

(Dated: 12 October 2022)

The shapes of rotating fluid drops held together by surface tension is an important field of study in fluid mechanics. Recently, experiments with micron-scale droplets of liquid helium have been undertaken and it has proven useful to compare the shapes of the resultant superfluid droplets with classical analogs. If the helium is a mixture of He^3 and He^4, two phases are present. In a recent paper, the shapes of rotating two phase fluid droplets were calculated where the inner drop was constrained to stay at the drop center. The outer shapes and dimensionless rotation rate-angular momentum relationships were shown to be similar to single phase drops provided that the density and surface tension scales were chosen appropriately. In the current paper, I investigate models in which the inner drop can displace from the centre. In order to simplify the analyses, two dimensional drops are first investigated. I show that the inner drop is unstable in the centre position if its density is greater than the outer density and that the inner drop will move towards the outer boundary of the drop in these cases. When the inner drop has a higher density than the outer drop, the moment of inertia of displaced inner drops is increased relative to centered drops and hence the kinetic energy is decreased. Shapes of two and three dimensional drops, rotation rate-angular momentum and kinetic and surface energy relationships are investigated for off-axis inner drops with parameters relevant to recent liquid He experiments.

Two-phase rotating fluid drops with inner drop displacement

I. INTRODUCTION

The shapes of rotating fluid drops help together by surface tension have been of interest for their own sake[1–7] but also because of analogies to celestial bodies held together by gravity[8] and atomic nuclei[9]. Spashform tektites are glassy rocks that are believed to have formed from rotating fluid drops resulting from large Earth impacts[10–13]. Experiments have recently been carried out in which microscopic liquid helium is expelled from a nozzle[14–17]. Liquid He^4 is a superfluid at the ultra-low temperatures at which these experiments are carried out. As a result, these drops carry their angular momentum in voritices if they are axisymmetric and in a combination of vortices and capillary waves if they are prolate[18] while classical viscous drops carry angular momentum through the net rotation of the drop. Nevertheless, the classical and super-fluid drops have many similarities in terms of their shape variations with angular momentum[19] and comparison of the two systems is useful in interpreting the results.

Recently, experiments and density functional theory calculations have been carried out on mixtures of He^3 and He^4 at temperatures where He^3 is a regular fluid while He^4 is a superfluid[20]. In these, the He^3 forms an outer shell of normal fluid surrounding an inner He^4 superfluid. The classical analog for this system is a drop made of a mixture of two immiscible fluids. In a recent paper, the shapes of rotating two phase drops were simulated numerically[21] and were shown to be very similar to single phase drops provided that an appropriate scaling was chosen. In that study, the initial condition for the inner drops was always centered on the rotation axis and so possible off-centered inner drops were not considered. However, recent experimental evidence suggests that the He^4 inner drop may not be centered (A. Vilesov, personal commuication, 2021) necessitating further numerical investigations of immiscible two phase drops.

As well as three dimensional (3D) drops, cylindrical fluids are studied here because of their simplicity relative to 3D drops. Cylindrical fluid domains and their stability to along-axis perturbations were studied by Rayleigh[22] in order to understand the process of jet break-up. The stability of rotating two-dimensional (2D) drops was later investigated[23,24]. It was shown that drops with a circular cross-section are stable up to a bifurcation rotation rate at which point two lobed shapes become stable. The shapes of these drops as a function of angular frequency for drops forced at a fixed rotation rate, or as a function of angular momentum for freely rotating drops, was later derived[25]. The behavior of 2D drops is similar to that of 3D drops in that both become non-axisymmetric above a bifurcation angular momentum. However, for all angular momenta below

the bifurcation value, 2D drops all have the same (circular) form while 3D drops are ellipsoids that become increasingly flattened with increasing angular momentum. This simplification of drop shape in 2D is useful in investigating the effects of mobile inner drops. Additionally, the current contribution represents the first numerical model results corroborating those of *Benner et al.* (1991). Two dimensional superfluid drops have also been investigated using density functional theory[19].

In what follows I will first briefly describe the numerical model used to calculate the shapes of equilibrium drops. I will then present some simple analyses of the energy of two phase, 2D, drops to show that the energy is minimized for centered inner drops when the inner drop has density less than the outer drop while off-centre inner drops are minima for denser inner phases. I will then show numerical model results comparing single phase, two phase with centered inner drop, and two phase with mobile inner drop results for 2D and 3D simulations for parameters relevant to the He^4-He^3 system.

II. THEORY

A. Governing Equations

The fluid drops are simulated by solving the Navier-Stokes equations in a reference frame that is co-rotating with the drop with two domains. In dimensionless form these are

$$\rho_i \frac{D\mathbf{u}}{Dt} = -\nabla P + \frac{O_h}{2}\nabla^2\mathbf{u} + \rho_i \omega^2 \mathscr{R}\hat{\mathbf{r}} \tag{1}$$

and

$$\nabla \cdot \mathbf{u} = 0, \tag{2}$$

in which the terms represent the dimensionless inertial, pressure gradient, viscous and centrifugal forces per unit volume. Here $\mathbf{u}$ and P are the velocity field and pressure while ρ_i is the dimensionless density of phase i. Symbols $\mathscr{R}$ and $\hat{\mathbf{r}}$ represent the distance from the rotation axis and a unit vector in the direction radially away from the rotation axis. Dimensionless numbers include the dimensionless angular rotation rate ω and the Ohnesorge number O_h. Note that while effects due to centrifugal forces have been included (the last term in equation 1), effects due to Coriolis forces have been neglected. These latter forces are zero for zero velocity and will not affect the final equilibrium shapes that are of interest here.

Two-phase rotating fluid drops with inner drop displacement

The inner boundary moves with the normal component of the velocity field and the normal component of the velocity field is continuous across the inner boundary while the position of the outer boundary moves with the normal component of the velocity. Surface tension causes a discontinuity in the normal stress on the inner boundary which is proportional to the curvature of the boundary

$$\hat{\mathbf{n}} \cdot \mathbf{T_{in}} - \hat{\mathbf{n}} \cdot \mathbf{T_{out}} = \frac{\sigma_{in}}{\sigma_{eff}} \nabla \cdot \hat{\mathbf{n}}/8. \tag{3}$$

Here, $\mathbf{T_{in}}$ and $\mathbf{T_{out}}$ indicate the dimensionless fluid stress tensors in the inner and outer regions, $\hat{\mathbf{n}}$ is a unit vector normal to the boundary while σ_{in} is the interfacial surface tension coefficient and σ_{eff} is the surface tension scale that will be defined below. On the outer boundary, surface tension causes a non-zero normal stress component

$$\hat{\mathbf{n}} \cdot \mathbf{T_{out}} = \frac{\sigma_{out}}{\sigma_{eff}} \nabla \cdot \hat{\mathbf{n}}/8 \tag{4}$$

where σ_{out} is the surface tension coefficient between the outer fluid and air or vacuum. With this boundary condition, the pressure outside the drop is assumed to be 0.

The dimensionless angular momentum L is a specified constant for each simulation. The dimensionless angular momentum is updated at each time step using

$$\omega = \frac{L}{I_{in} + I_{out}} \tag{5}$$

where I_{in} and I_{out} are the dimensionless moments of inertia calculated from

$$I_i = \int \rho_i \mathscr{R}^2 dV_i, \tag{6}$$

where i is an index over the inner and outer regions.

B. Non-dimensionalization

The length scale for non-dimensionalization is the outer radius of the circle of equal area (for 2D drops) or the sphere of equal volume (for 3D drops), R_{out}. Time and pressure are scaled as $\sqrt{\rho_{eff} R_{out}^3 8^{-1} \sigma_{eff}^{-1}}$ and $8\sigma_{eff} R_{out}^{-1}$. Angular momentum, energy and moment of inertia are scaled by $\sqrt{8\sigma_{eff}\rho_{eff} R_{out}^{2n+1}}$, $8\sigma_{eff} R_{out}^{n-1}$ and $\rho_{eff} R_{out}^{n+2}$ where $n = 2$ and 3 for 2D and 3D drops respectively. In 2D simulations, these are the respective quantities per unit length perpendicular to the domain. The density scale is chosen to be

$$\rho_{eff} = \frac{\rho_{in} R_{in}^{n+2} + \rho_{out}(R_{out}^{n+2} - R_{in}^{n+2})}{R_{out}^{n+2}}. \tag{7}$$

Here R_{in} is the radius of a circle of equal area or sphere of equal volume for the inner drop for 2 and 3D calculations. This choice insures that the dimensionless moment of inertia of undeformed drops is the same as for a single phase drop of density ρ_{eff}. The surface tension scale is given by

$$\sigma_{eff} = \frac{\sigma_{in} R_{in}^{n-1} + \sigma_{out} R_{out}^{n-1}}{R_{out}^{n-1}}. \tag{8}$$

This choice results in the total dimensionless surface energy for undeformed inner and outer drops being independent of material properties and drops sizes. Note that this is a different choice for the nondimensionalization than I used previously[21]. However, as will be shown, the angular frequency and kinetic and surface energy variations with angular momentum remain similar to those for single phase drops.

The Ohnesorge number is given by

$$O_h = \eta (2\rho_{eff}\sigma_{eff}R_{out})^{-1/2} \tag{9}$$

where η is the liquid viscosity which is assumed constant. The Ohnesorge number represents the ratio of viscous to surface tension forces and can be thought of as a damping parameter for surface oscillations. All of the simulations in the current paper used $O_h = 1$ which roughly represents critical damping.

I characterize the inner drop using three additional dimensionless numbers, $s = \sigma_{in}/\sigma_{out}$, $p = \rho_{in}/\rho_{out}$ and $r = R_{in}/R_{out}$. Additionally, the inner drop's initial position was displaced from the centre by dimensionless distance x_{in0}.

Simulations were initiated with drops with elliptical cross-sections with semi-major axis $(1+\delta)$ and semi-minor axis $(1+\delta)^{-1}$ where δ was given value 0.01. This perturbation to a circular or spherical profile acted as a seed for the non-axisymmetric instability. The dimensionless numbers characterizing the problem are summarized in table II B.

C. Numerical Model

The numerical model has been described previously[21], however, it is modified to simulate 2D drops. Briefly, the time-dependent equations are run to steady-states in order to find stable equilibrium states. The Microfluidics Module capabilities of the commercial finite element package,

Two-phase rotating fluid drops with inner drop displacement

Symbol	Description	Value 2D	Value 3D
L	Dimensionless angular momentum	0-2	0-2
O_h	Ohnesorge Number	1	1
p	Inner-outer density ratio	1.78	1.78
r	Inner-outer radius ratio	0.5348	0.5348
s	Inner-outer surface tension ratio	0.14159	0.14159
x_{in0}	Initial inner drop position	0 or 0.1	0 or 0.2
δ	Initial drop ellipticity	0.01	0.01

TABLE I. A summary of the problem dimensionless numbers.

Comsol Multiphysics[26], is used with an Arbitrary Euler-Lagrange method (included in Comsol as a Deforming Mesh) which is used to allow for the deforming domain. Hyperelastic smoothing is used to determine the updated locations of the deforming mesh. In *Butler* (2020)[21], the inner and outer drops had initial centres at the origin ($x_{in0} = 0$). In the current investigation, the initial positions of the inner and outer drops were moved from the central position.

The equations are solved on triangular (2D) and tetrahedral (3D) meshes. The meshes consisted of roughly 3000 (2D) and 9000 (3D) elements. Automatic remeshing was used such that a new reference mesh was created when the minimum element quality fell below a threshold. Direct solvers Multifrontal Massively Parallel Sparse Direct Solver (MUMPS)[27] and Parallel Sparse Direct Solver (PARDISO)[28] were used for the 2 and 3D simulations while Backward Differentiation Formula (BDF)[29] time-stepping was used. A numerical instability often resulted in a net force on the drops and so they translated in a particular direction. This instability was particularly pronounced in 3D simulations. In order to reduce this runaway, the average force on the drop was subtracted from the body force at all positions.

D. Centre of Mass

The centre of mass of an isolated drop will remain fixed when analyzed in an appropriate reference frame. When the inner drop is allowed to move, the centres of inner and outer drops change with time, however. Considering only drop displacements along the x axis, the centre of mass for 2D (circular) and 3D (spherical) drops can be written in terms of the centres of the inner

Two-phase rotating fluid drops with inner drop displacement

and outer drops, x_{in} and x_{out} as

$$x_{cm} = \frac{x_{in} r^n (p-1) + x_{out}}{r^n (p-1) + 1}, \tag{10}$$

where again $n = 2$ and 3 for 2 and 3D drops.

The centre of mass of the system will not move and so if we set up the system with $x_{cm} = 0$ then we can set equation 10 to 0 to get a relationship between the centres of the inner and outer drops

$$x_{out} = -x_{in} r^n (p-1). \tag{11}$$

The parameter x_{in} was selected as an initial condition for each simulation and equation 11 was used to select the appropriate initial value for x_{out}.

E. Energy

Stable drops will be those that minimize the total energy[3]. In the general case, there is a trade-off between decreasing the kinetic energy, E_k, by increasing the moment of inertia and increasing the surface energy, E_s, as the drop deforms. The dimensionless total energy for 2 and 3 D drops is given by

$$E_{tot} = \frac{1}{2} \frac{L^2}{I_{in} + I_{out}} + \frac{C_{in} s + C_{out}}{8(s r^{n-1} + 1)}, \tag{12}$$

where C_{in} and C_{out} are the circumferences of the drops for 2D drops and their surface areas for 3D drops.

While single phase 3D drops are deformed for all angular momenta greater than zero[2], 2D single phase drops remain circular in cross-section for angular momenta up to 0.96[25]. For 2D 2 phase co-centric drops, the pressure and centrifugal force fields will be axially symmetric and so the inner and outer drops will similarly be circular. If the inner drop is displaced from the center, the inner and outer drops may deform from circular cross-sections. In this section, I will consider simple circular drops in order to get insight into drop stability.

When outer and inner 2D drops have circular cross-section, but are not necessarily concentric, the energy reduces to

$$E_{tot} = \frac{1}{2} \frac{L^2}{I_{in} + I_{out}} + \frac{\pi}{4}. \tag{13}$$

Note that given the nondimensionalization for the surface tension in equation 8, the only dimensionless number on which equation 13 depends explicitly is L. We can see that for inner and

outer drops of circular cross section and fixed area, all of the terms in equation 13 are constant except for I_{in} and I_{out} and that minimizing E_{tot} amounts to maximizing $I_{in}+I_{out}$. The moments of inertia of the drops will be functions of their positions relative to the rotation axis. The centre of mass of the inner drop will be the same as the centre of the inner drop circle. The centre of mass of the outer drop will not be the same as the that of the large circle, however. I consider a situation where the inner drop is displaced along the x axis only.

For the inner drop, we can use the parallel axis theorem[30] to show that the contribution to the moment of inertia for a rotation about x_{cm} is

$$I_{in} = \frac{\pi p(\frac{r^4}{2} + x_{in}^2 r^2)}{pr^4 + (1-r^4)}, \tag{14}$$

while for the outer circle it is

$$I_{out} = \frac{\pi(\frac{1}{2} + x_{out}^2 - \frac{r^4}{2} - x_{in} r^2)}{pr^4 + (1-r^4)}. \tag{15}$$

The combined moment of inertia is then

$$I_t = \frac{\pi[\frac{1}{2} + x_{out}^2 + (p-1)(\frac{r^4}{2} + x_{in} r^2)]}{pr^4 + (1-r^4)}. \tag{16}$$

Note that equation 16 reduces to the single phase moment of inertia if $p = 1$. Note also that if $p < 1$, equation 16 has a maximum for $x_{in} = 0$ while it increases quadratically in x_{in} when $p > 1$. As a result, for circular drops, which will generally obtain for low angular momenta, the lowest energy state will occur with the inner drop centered when $p < 1$ while the inner drop will move towards the outer edge when $p > 1$.

As will be shown, when the inner drop approaches the outer edge, the shapes of the inner and outer drops deform significantly and the surface energy terms increase. Additionally note that for centered drops with $x_{in} = x_{out} = 0$ that I_t reduces to $\pi/2$ for any value of p and so the total energy becomes

$$E_{tot} = \frac{L^2}{\pi} + \frac{\pi}{4}. \tag{17}$$

So, for centered circular inner drops, which will occur when $p < 1$ and $L < 0.96$, the total energy will simply be quadratic in the angular momentum and is independent of s, r and p provided that the nondimensionalizations in equation 7 and 8 are used. This function is plotted as the magenta line in figure 1.

III. RESULTS

A. Single Phase 2D drops

In order to test the 2D numerical model, single phase simulations were first run. Additionally, to my knowledge, these are the first published numerical simulation results for 2D rotating drops. The results for the angular velocity vs angular momentum are shown in figure 2 where the blue line represents the results of *Benner et al* (1991) (there is a factor of 2 difference in the nondimensionalization of L) while the blue square symbols represent the results from the current study. The straight line for $L < 0.96$ indicates that the drops do not deviate from their circular cross section and so their moment of inertia remains unchanged over this range. *Benner et al* (1991) found that ω at the bifurcation point was $(3/8)^{1/2} \approx 0.6124$ while my simulations found 0.616. The drops become unstable to a nonaxisymmetric disturbance at $L > 0.96$ and take on two lobed shapes with significantly larger moments of inertia, leading to the decrease in ω with L above the bifurcation point. A high density of simulations were run near $L = 0.96$ in order to better constrain the bifurcation rotation rate.

Figure 1 (blue, red and magneta dotted lines) shows the kinetic, surface and total energies (the terms in equation 17) for a drop of circular cross-section rotating with angular momentum L . The solid blue, red and magenta lines show the kinetic, surface and total energies for 2D single phase drops from my simulatinos. Above the bifurcation angular momentum, the kinetic energy increases more slowly with L than for a circular drop as the drop becomes nonaxisymmetric and mass is moved away from the origin. Below the bifurcation angular momentum, the surface energy is constant but it increases rapidly above it, again as the drop becomes non-axisymmetric and the circumference increases compared with a circle.

Figure 3 shows the pressure field within the equilibrium single phase 2D drops for a range of angular momenta. Below $L = 0.96$, the drops have a circular cross-section and the pressure difference between the outer edge of the drop and the center increases as the rotation rate and the centrifugal force increases

Above $L = 0.96$, the drops differ from circular and become increasingly prolate with increasing L. The pressure is no longer axisymmetric and is maximal at the end of the long axis where the curvature of the drop is greatest. Above $L = 1$, the drops begin to thin at the equator giving them negative curvature and pressures less than the outside pressure even on the outer edges. Note

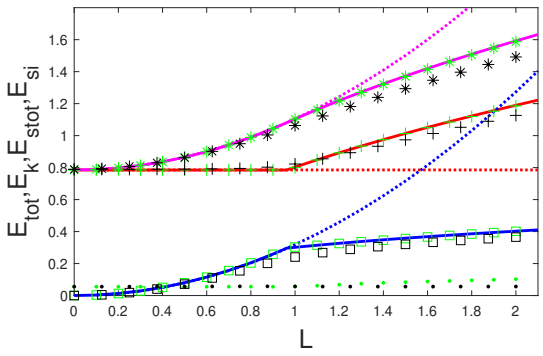

FIG. 1. The total, E_{tot}, (magenta dotted and solid lines, green and black asterisks), kinetic, E_k (blue dotted and solid line, green and black squares) and total surface, E_{stot} (red dotted and solid lines, green and black + symbols) energies for a circular single or two phase drop, a single phase deforming drop, a two phase drop with central inner drop and two phase drops with mobile inner drop, respectively. Green and black dots show the surface energy, E_{si}, of the inner drops for fixed and mobile cases.

also that the total pressure difference becomes almost independent of L for L greater than 1.25. In equilibrium, inside the drop, the centrifugal force is balanced by the pressure gradient. The rotation rate decreases gradually with L for L above the bifurcation angular momentum, decreasing the resulting pressure gradient along the long axis of the drop. However, the drop also becomes longer in such a way as to keep the total pressure difference close to constant which also means that the maximum curvature at the tip of the drop is similar for prolate drops with different L. In the short axis direction through the center of the drop, the thickness decreases with L at the same time as the rotation rate, leading to the pressure becoming almost constant in the short axis direction for the $L = 2$ simulation.

Benner et al.(1992) showed that single phase drops will break-up as the central neck thins and eventually goes to 0 for values of L around 3. The ALE method is not well suited to studying drop break-up because it cannot simulate a change in topology. Some single phase simulations were run with values of L near 3 and the central neck did become extremely thin (not shown) and for some higher values, the simulations failed to converge, consistent with drop break up.

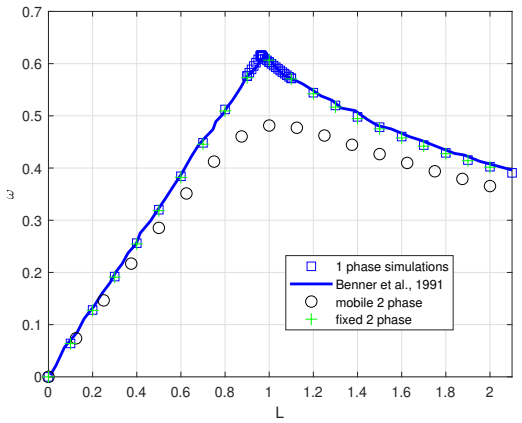

FIG. 2. Comparison of the variation of rotation rate with angular momentum for 1 phase, 2 phase with the centre fixed and 2 phases with a mobile centre.

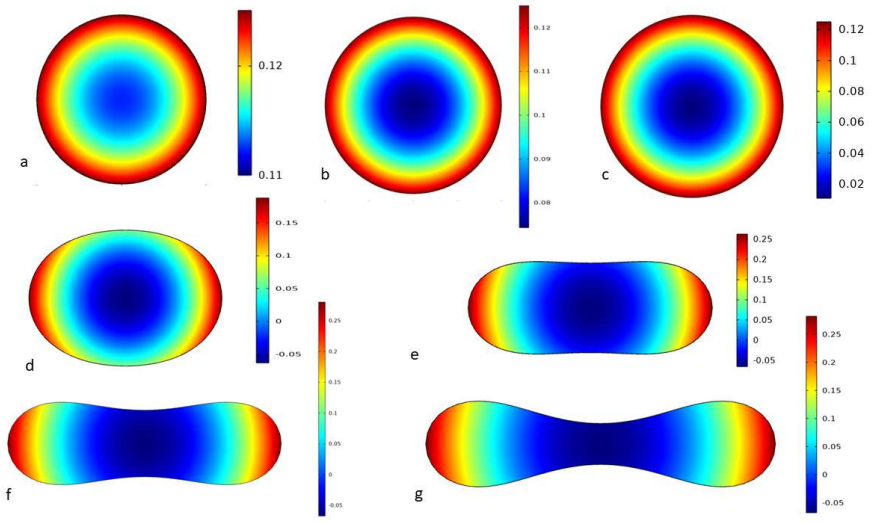

FIG. 3. The dimensionless pressure in single phase drops for angular momenta a) 0.25, b) 0.5, c) 0.75, d) 1 e) 1.25 f) 1.5 and g) 2.

B. Two Phase 2D drops

Because of the relevance to the liquid helium problem, I concentrate here on dimensionless parameter values $p = 1.78$, $s = 0.14159$ and $r = 0.5348$[20].

1. Two phase, fixed centre, 2D drops

A first set of simulations were undertaken with $x_{in0} = 0$ and regardless of the value of p, the inner drops remained centered for an extended period of time. In some simulations, if run for long enough, numerical instabilities eventually resulted in the inner drop displacing towards the outer surface and in some others the central drop eventually broke into two drops connected by a thin filament. The ALE method is unable to simulate a change in topology such as a drop breaking into two. That the inner drop remained centered and unchanging for an extended period indicates that centered drops represent an equilibrium state, albeit a possibly unstable one. The total energy and angular rotation rate for the fixed centered drops are shown by the green symbols in figure 1 and 2 for drops with $p = 1.78$, $s = 0.14159$ and $r = 0.5348$. Using the nondimensionalization of the current paper, the variation of total energy and angular rotation rate with angular momentum is essentially unchanged from the single phase case. For these values of p, s and r, it can also be seen that the kinetic energy and surface energy (the sum of the inner and outer drop surface energies) are essentially the same as for a single phase drop.

In figure 4, the pressure field is shown for the fixed centered calculations. The drop shape evolution with L as well as the total pressure difference within the drops is very similar to those for single phase drops. In the presence of the inner drop, there is a pressure discontinuity at both the outer boundary and the inner one. At $L = 0.25$ (figure 4a), the pressure variation due to the centrifugal force is small compared with the discontinuities due to surface tension and the pressure fields are close to constant in the inner and outer drop regions. The maximum pressure is also found within the inner drop. As L increases but for values less than the bifurcation angular momentum, the centrifugal forces increase and the pressure differences required to balance these similarly increase and become greater than the pressure discontinuity at the inner drop boundary.

For $L > 0.96$, both the inner and outer drops become prolate and have similar shapes. *Butler* (2020) found that the outer shapes of 3D two phase drops were very similar to those for single phase drops. However, the shape of the inner drop varied significantly particularly for small values

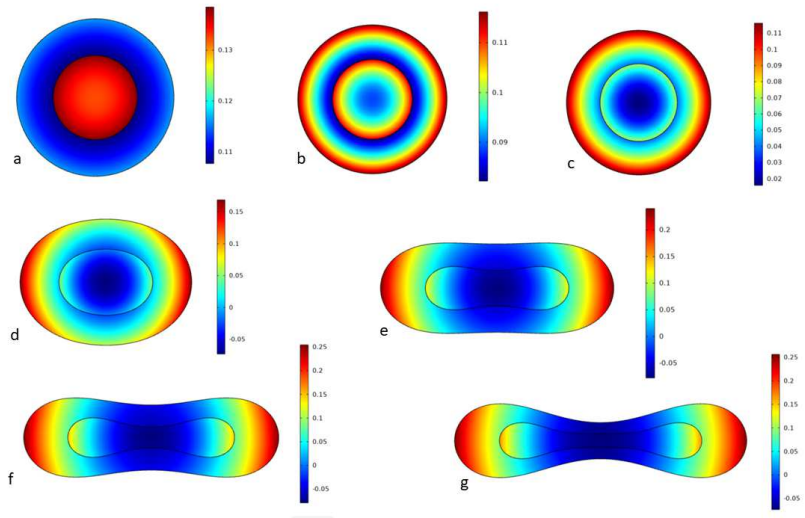

FIG. 4. The dimensionless pressure in two phase drops with fixed central drop for angular momenta a) 0.25, b) 0.5, c) 0.75, d) 1 e) 1.25 f) 1.5 and g) 2.

of r. When s was large and p small, the inner drops were often close to spherical due to significant inner surface tension effects and little centrifugal forces in the inner drop. Drops with small s and large p, such as the those simulated here, took on shapes similar to the outer drops as seen here.

2. *Mobile Inner Drops, 2D*

A subsequent set of simulations were undertaken with $x_{in0} = 0.1$. Equation 11 was then used to set the initial position of the outer drop so that the initial value of $x_{cm} = 0$. Simulations were first undertaken with $p < 1$. In these cases, the inner drop returned to the centre as is predicted by the maximum of the moment of inertia. Subsequent simulations were undertaken with $p > 1$ and in these cases, the inner drop displaced towards the outer surface.

The time evolution of a drop with $L = 2$ is shown in figure 5. Shapes of the inner and outer drops are shown at the times indicated where colors indicate the pressure field while magenta arrows show the fluid velocity. The drop has become prolate by time 10. Subsequently, the inner drop slowly migrates to the right outer surface, forming at time 700 a narrow neck connecting its

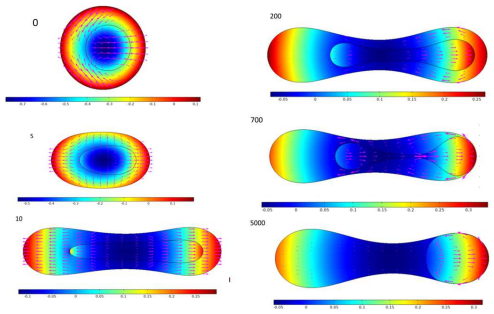

FIG. 5. The shapes for a drop with parameters $p = 1.78$, $s = 0.14159$ and $r = 0.5348$ $x_{onin} = 0.1$, $L = 2$ and O_h at the times indicated. Colors indicate the pressure while magenta arrows show the velocity field. Velocity arrows are scaled by the maximum velocity. At time 5000, there is still small magnitude fluid motion but the drop has essentially obtained its final shape.

two ends. The timescale for the nonaxisymmetric instability to evolve the outer drop to a prolate shape is clearly shorter than the timescale for the inner drop to migrate to one side or the other. Since the principal aim of this investigation was calculating equilibrium shapes, effects of Coriolis and Poincare forces were neglected. With their inclusion, the time evolution of the drops may have been somewhat different.

Figure 6 shows the results of simulations with $p = 1.78$, $s = 0.14159$ and $r = 0.5348$ for angular momenta $L = 0.25, 0.5, 0.75, 1, 1.25, 1.5, 1.75$ and 2. The simulations have been run to equilibrium. Figures 1 and 2 (black circles) show the corresponding energies and angular rotation rates as a function of the angular momentum.

At $L = 0.25$, the outer drop remains close to circular and the energy and angular rotation rates are very similar to those for a single phase drop even though the inner drop has displaced close to the outer boundary. Similar to the centered inner drop case, pressure variations are dominated by the discontinuity at the inner drop boundary. However, even at this low angular momentum, the inner drop has deformed from a circular shape. At $L = 0.5$, the outer and especially the inner drops have become significantly deformed from circular. The additional curvature of the outer drop can be seen to be causing an enhanced pressure gradient near the wall of the outer drop and is keeping the inner drop in. The increase in the moment of inertia caused by moving the inner drop to the outer boundary can be seen as causing a decrease in the angular rotation rate compared with a

single phase drop. By $L = 0.75$, the outer drop has become visibly different from circular despite the angular momentum being less than 0.96 and the angular rotation rate is considerably decreased from that of a single phase drop. For $L = 1$, the kinetic energy of the mobile drop is noticeably less than for the fixed case while the surface energy is slightly higher due to the increased deformation of the outer surface. In figure 2 it can be seen that for mobile inner drops, there is no longer a cusp in the L vs ω curve as the drops transition more gradually from circular to prolate forms. For angular momenta above 1.25, both the kinetic energy and the surface energies are reduced for the mobile drop case compared with the fixed drop case. This is at least partially due to the lower surface energy of the inner drop which is closer to circular at high L than the fixed drop cases.

The simulations shown were all run with the semi-major axis of the initial outer drop along the same axis (the x axis) as the displacement of the inner drop from the centre. Some simulations (not shown) were undertaken with the semi-major axis at 90, 45 and 22.5 $^\circ$ to the initial displacement of the inner drop. The simulations at 22.5 and 45° showed identical results to those shown here. At high angular momenta, when the outer drop was prolate, for simulations where the semi-major axis was exactly perpendicular to the initial inner drop displacement, the inner drop became symmetrically split between the two outer lobes and was connected by a narrow filament. For real drops, it would be unlikely that the non-axisymmetric perturbation would occur exatly 90° to the inner drop displacement and so the splitting of the inner drop would be unlikely to occur.

Some simulations (not shown) were run with $O_h = 0.1$. In these simulations, both the inner and outer drops oscillate significantly but eventually settled to the same equilibrium state as was found in the simulations run with $O_h = 1$. Additionally, simulations were run with $O_h = 0.1$ in the inner drop and 1 in the outer region. As expected, although the time variation differed from drops with constant viscosity, the final state was unchanged. A simulations was also run with $p = 2.67$ and $L = 2$. The final shape of the drop was very similar to the simulation using $p = 1.78$.

C. Three Dimensional Drops

In figure 7, the total (magenta line), surface (red line) and kinetic (blue line) energies for single phase equilibrium 3D drops are shown as a function of angular momentum. For 3D drops, the bifurcation angular momentum occurs for L close to 1.2. Unlike 2D drops, the drops increasingly deform up to the bifurcation angular momentum leading to the slight increase in the surface energy up to that point. Above $L = 1.2$, the surface energy increases rapidly while the kinetic energy be-

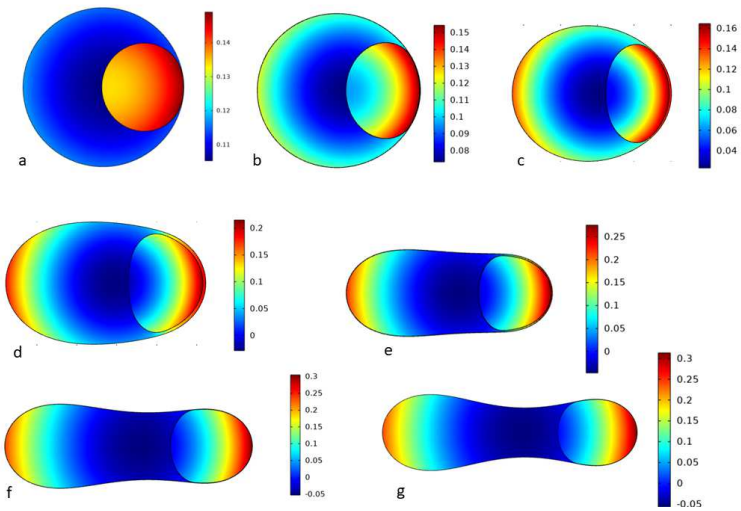

FIG. 6. Examples of 2D drop shapes at angular momenta a) 0.25, b) 0.5, c) 0.75, d) 1, e) 1.25, f) 1.5, and g) 2. Colors indicate the pressure.

comes close to constant as drops become increasingly prolate and their surface areas and moments of inertia increase rapidly. Figure 8 shows the variation of ω with L and similar to the 2D case, the cusp in the curve at the bifurcation angular momentum is not present when the inner drop is mobile.

Simulations were run with $p = 1.78$, $s = 0.14159$ and $r = 0.5348$ and $x_{in} = x_{out} = 0$ and, like for the 2D simulations, the inner drops remained centered for extended periods of time. The resulting energies of equilibrium drops are shown in figure 7 and the angular rotation rate is shown in figure 8 with the green symbols. The surface energy associated with the inner drop is shown by the dots while the sum of the surface energies of the inner and outer drops is shown by the '+' symbols. The dimensionless energies and angular rotation rates are essentially the same for fixed-centre two phase drops as those for single phase drops.

These simulations were then repeated with $x_{in} = 0.2$ (black symbols in figures 7 and 8). The kinetic energy is slightly reduced for mobile central drops relative to fixed central drops particularly near $L = 1$. Slices of the pressure field at different angular momenta are shown in figure 9. Near $L = 1$, the drop with a mobile central drop has become prolate while at this angular momen-

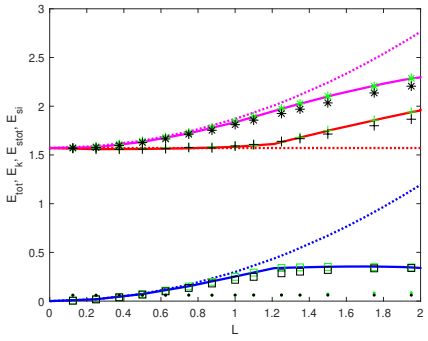

FIG. 7. For 3D drops, the total, E_{tot}, (magenta solid line, green and black asterisks), kinetic, E_k (blue solid line, green and black squares) and total surface, E_{stot}, (red solid line, green and black + symbols) energies for a single phase rotating drop, two phase drop with central inner drops and two phase drops with mobile inner drop, respectively. Green and black dots show the surface energy of the inner drops, E_{si}, for fixed and mobile inner drops. Dotted lines show E_k (blue), E_{stot} (red) and E_{tot} (magneta) for an undeformed uniform sphere.

tum, single phase and two phase drops with fixed central drops (not shown) remain oblate and have smaller moments of inertia. At L approaching 2, the kinetic energy for the mobile drop case becomes similar to the fixed centre drop case while the surface energy is slightly reduced. At this high angular momentum, the drops are prolate, however, the inner drop is found in only one end. The end of the drop not containing the inner drop is not as strongly deformed as a case with no inner drop leading to the reduction in surface energy. In all cases, the total energies of the mobile inner drop simulations are slightly lower than those for fixed centre drops. It can also be seen that the aspect ratio of 3D prolate drops is less than for 2D drops with the same angular momentum and that the pressure difference within the drops is larger for the 3D drops. Both of these effects can be understood to occur because there is curvature in two directions for 3D drops which roughly doubles the pressure drop across the interfaces and reduces deformation.

IV. CONCLUSIONS

Modeling of two dimensional rotating liquid drops with surface tension has been carried out and the resulting angular momentum - angular velocity relationship has been shown to be in good

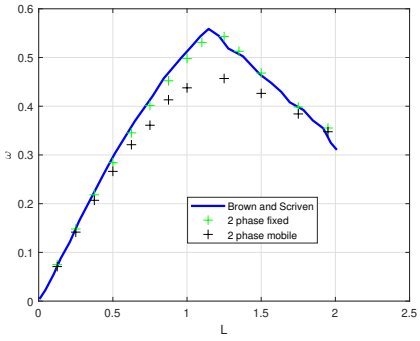

FIG. 8. For 3D drops, angular rotation rate as a function of angular momentum for single phase drops (digitized results of Brown and Scriven) as well as two phase drops with fixed (green symbols) and mobile (black symbols) inner drops. $p = 1.78$, $s = 0.14159$ and $r = 0.5348$ for the two phase drops.

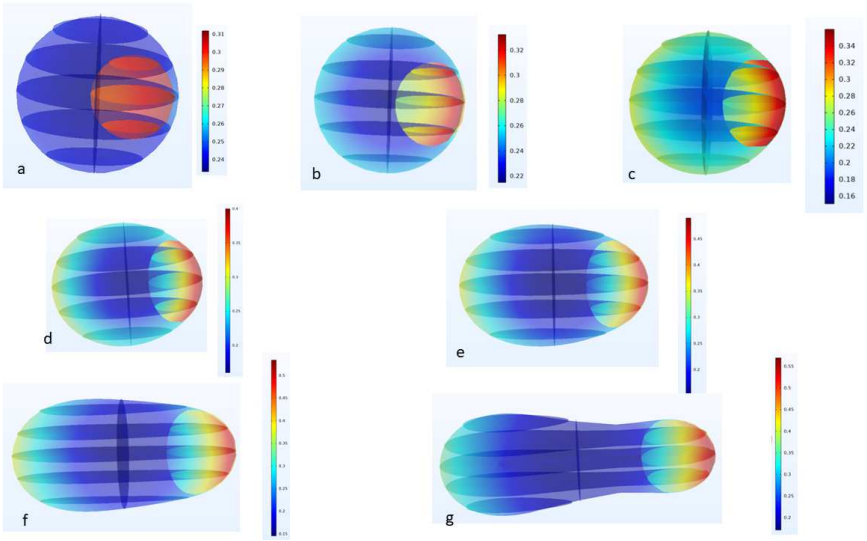

FIG. 9. Slice plots of the pressure field for 3D drops. The view is tilted slightly from the rotation axis. $p = 1.78$, $s = 0.14159$ and $r = 0.5348$ a) $L = 0.25$, b) $L = 0.5$, c) $L = 0.75$ d) $L = 1$ e) $L = 1.25$ f) $L = 1.5$ g) $L = 2$. There is one slice in the plane perpendicular to rotation and in the plane contaning the rotation axis perpendicular to the displacement of the inner drop. There are five planes perpendicular to these two directions.

agreement with the predictions of *Benner and Scriver* (1991)[25] for single phase drops. A simple examination of the moment of inertia for 2D two phase circular drops showed that the minimum energy occurs when the drops are cocentric when the inner drop fluid is less dense than the outer fluid while the energy decreases as the drop moves towards the outer edge when the inner drop is more dense. For rotating drops, the centrifugal force plays a role that is analogous to gravity and causes a buoyancy force where light drops move to the centre and heavy ones move to the outer edge. When the inner drop is more dense, centered inner drops represent equilibrum states but there exist lower energy states for inner drops displaced close to the outer edges. As such, I expect that rotating two phase drops, where the inner drop is more dense, will always be found with the inner drop close to the outer boundary. In a previous paper[12], I investigated 3D two phase drops but in all cases, the inner drop was centered and models were not run for sufficiently long periods of time that numerical errors combined to perturb the drop from its central position which would lead to denser inner drops then displacing to the outer boundary.

The behaviours of two and three dimensional 2 phase drops are broadly similar in terms of their rotation rate- angular momentum relations, energy variation with angular momentum and shape variations with angular mometum. Because 3D drops have curvature in two directions while 2D drops have curvature in only one, 2D drops deform to a greater extent from circular cross sections than 3D drops do from spheres.

In *Butler* (2020)[21], I showed that the dimensionless angular momentum-angular velocity relationship was similar for single phase and two phase drops provided that the density and surface tension were scaled appropriately. In that paper, the density scale was chosen so that the moment of inertia for the two phase drops was the same as a single phase drop for a sphere while the surface tension scale was chosen empirically as a the weighted average of the inner and outer surface tension coefficients where the weights were the radii of the inner and outer drops. In the current paper, the density scale was generalized for 2D as well as 3D drops while the surface tension scale was chosen so as to give the same total dimensionless surface energy for two phase and single phase drops. For the parameters investigated, the 2D and 3D angular momentum-angular velocity relations as well as the variation of the total, surface and kinetic energies with angular momentum were very similar for fixed-center two phase drops and single phase drops. These relations for mobile drops were somewhat different as the displacement of the inner drop increased the moment of inertia and changed the total deformation. I believe that the scalings used in the current paper are the most useful in investigating two phase drops as they allow easy and meaningful comparisons

of the kinetic and surface energies.

Insights from the current paper on classical two phase drops will be useful in interpreting results for He^3-He^4 two phase droplets. Since the more dense He^4 has the higher vacuum surface tension, it is expected that it will make up the inner drop. As such, if the classical analogy for these drops holds, I expect that the inner drops will be displaced from the drop center. Results in the current paper show that when the inner drops displace from the center, at high angular momenta, the drops lose their symmetry about a reflection through their centers in a plane perpendicular to their long axes. Additionally, when drops can displace from the center, the transition from oblate to prolate forms with angular momentum becomes more gradual – these effects that may be seen in these experiments.

V. ACKNOWELEDGEMENTS

I would like to acknowledge Marti Pi, Francesco Ancilotto and Manuel Barranco and Andrey Vilseov for their helpful discussions on this topic.

VI. DATA AVAILABILITY

The data that support the findings of this study are available from the corresponding author upon reasonable request.

REFERENCES

[1]S. Chandrasekhar, "STABILITY OF A ROTATING LIQUID DROP," PROCEEDINGS OF THE ROYAL SOCIETY OF LONDON SERIES A-MATHEMATICAL AND PHYSICAL SCIENCES **286**, 1–& (1965).

[2]R. Brown and L. Scriven, "The shape and stability of rotating liquid-drops," PROCEEDINGS OF THE ROYAL SOCIETY OF LONDON SERIES A-MATHEMATICAL PHYSICAL AND ENGINEERING SCIENCES **371**, 331–357 (1980).

[3]S. Cohen, F. Plasil, and W. Swiatecki, "EQUILIBRIUM CONFIGURATIONS OF ROTATING CHARGED OR GRAVITATING LIQUID MASSES WITH SURFACE-TENSION .2." ANNALS OF PHYSICS **82**, 557–596 (1974).

[4]P. Luyten and D. Callebaut, "Stability of rotating liquid-drops .1. uncharged drops," PHYSICS OF FLUIDS **26**, 2359–2367 (1983).

[5]H. Ishikawa and K. Nishinari, "Modelling levitated 2-lobed droplets in rotation using Cassinian oval curves," JOURNAL OF FLUID MECHANICS **846**, 1088–1113 (2018).

[6]T. Wang, E. TRINH, A. CROONQUIST, and D. ELLEMAN, "Shapes of rotating free drops - spacelab experimental results," PHYSICAL REVIEW LETTERS **56**, 452–455 (1986).

[7]T. Wang, A. ANILKUMAR, C. LEE, and K. LIN, "Bifurcation of rotating liquid-drops - results from usml-1 experiments in-space," JOURNAL OF FLUID MECHANICS **276**, 389–403 (1994).

[8]V. Cardoso and L. Gualtieri, "Equilibrium configurations of fluids and their stability in higher dimensions," CLASSICAL AND QUANTUM GRAVITY **23**, 7151–7198 (2006).

[9]N. Bohr and J. Wheeler, "The mechanism of nuclear fission," PHYSICAL REVIEW **56**, 426–450 (1939).

[10]L. Elkins-Tanton, P. Aussillous, J. Bico, D. Quere, and J. Bush, "A laboratory model of splash-form tektites," METEORITICS & PLANETARY SCIENCE **38**, 1331–1340 (2003).

[11]M. R. Stauffer and S. L. Butler, "The Shapes of Splash-Form Tektites: Their Geometrical Analysis, Classification and Mechanics of Formation," EARTH MOON AND PLANETS **107**, 169–196 (2010).

[12]S. L. Butler, M. R. Stauffer, G. Sinha, A. Lilly, and R. J. Spiteri, "The shape distribution of splash-form tektites predicted by numerical simulations of rotating fluid drops," JOURNAL OF FLUID MECHANICS **667**, 358–368 (2011).

[13]K. A. Baldwin, S. L. Butler, and R. J. A. Hill, "Artificial tektites: an experimental technique for capturing the shapes of spinning drops," SCIENTIFIC REPORTS **5** (2015), 10.1038/srep07660.

[14]L. F. Gomez, K. R. Ferguson, J. P. Cryan, C. Bacellar, R. M. P. Tanyag, C. Jones, S. Schorb, D. Anielski, A. Belkacem, C. Bernando, R. Boll, J. Bozek, S. Carron, G. Chen, T. Delmas, L. Englert, S. W. Epp, B. Erk, L. Foucar, R. Hartmann, A. Hexemer, M. Huth, J. Kwok, S. R. Leone, J. H. S. Ma, F. R. N. C. Maia, E. Malmerberg, S. Marchesini, D. M. Neumark, B. Poon, J. Prell, D. Rolles, B. Rudek, A. Rudenko, M. Seifrid, K. R. Siefermann, F. P. Sturm, M. Swiggers, J. Ullrich, F. Weise, P. Zwart, C. Bostedt, O. Gessner, and A. F. Vilesov, "Shapes and vorticities of superfluid helium nanodroplets," Science **345**, 906–909 (2014), https://www.science.org/doi/pdf/10.1126/science.1252395.

[15]C. Bernando, R. M. P. Tanyag, C. Jones, C. Bacellar, M. Bucher, K. R. Ferguson, D. Rupp, M. P. Ziemkiewicz, L. F. Gomez, A. S. Chatterley, T. Gorkhover, M. Muller, J. Bozek, S. Carron, J. Kwok, S. L. Butler, T. Moller, C. Bostedt, O. Gessner, and A. F. Vilesov, "Shapes of rotating superfluid helium nanodroplets," PHYSICAL REVIEW B **95** (2017), 10.1103/PhysRevB.95.064510.

[16]B. Langbehn, K. Sander, Y. Ovcharenko, C. Peltz, A. Clark, M. Coreno, R. Cucini, M. Drabbels, P. Finetti, M. Di Fraia, L. Giannessi, C. Grazioli, D. Iablonskyi, A. C. LaForge, T. Nishiyama, V. O. A. de Lara, P. Piseri, O. Plekan, K. Ueda, J. Zimmermann, K. C. Prince, F. Stienkemeier, C. Callegari, T. Fennel, D. Rupp, and T. Moeller, "Three-Dimensional Shapes of Spinning Helium Nanodroplets," PHYSICAL REVIEW LETTERS **121** (2018), 10.1103/PhysRevLett.121.255301.

[17]F. Ancilotto, M. Barranco, and M. Pi, "Spinning superfluid He-4 nanodroplets," PHYSICAL REVIEW B **97** (2018), 10.1103/PhysRevB.97.184515.

[18]M. Pi, J. M. Escartín, F. Ancilotto, and M. Barranco, "Coexistence of vortex arrays and surface capillary waves in spinning prolate superfluid ^{4}He nanodroplets," Phys. Rev. B **104**, 094509 (2021).

[19]S. M. O. O'Connell, R. M. P. Tanyag, D. Verma, C. Bernando, W. Pang, C. Bacellar, C. A. Saladrigas, J. Mahl, B. W. Toulson, Y. Kumagai, P. Walter, F. Ancilotto, M. Barranco, M. Pi, C. Bostedt, O. Gessner, and A. F. Vilesov, "Angular momentum in rotating superfluid droplets," Phys. Rev. Lett. **124**, 215301 (2020).

[20]M. Pi, F. Ancilotto, J. M. Escartín, R. Mayol, and M. Barranco, "Rotating mixed ^{3}He $-^4$ He nanodroplets," Phys. Rev. B **102**, 060502 (2020).

[21]S. L. Butler, "Equilibrium shapes of two-phase rotating fluid drops with surface tension," PHYSICS OF FLUIDS **32** (2020), 10.1063/1.5134458.

[22]L. Rayleigh, "On the stability of jets," Proc. Long. math. Soc.. **1**, 361–371 (1879).

[23]L. Hocking and D. Michael, "The stability of a column of rotating liquid," Mathematika **6**, 25–32 (1959).

[24]L. Hocking, "The stability of a rigidly rotating column of liquid," Mathematika **7**, 1–9 (1960).

[25]R. BENNER, O. BASARAN, and L. SCRIVEN, "Equilibria, stability and bifurcations of rotating columns of fluid subjected to planar disturbances," PROCEEDINGS OF THE ROYAL SOCIETY OF LONDON SERIES A-MATHEMATICAL PHYSICAL AND ENGINEERING SCIENCES **433**, 81–99 (1991).

[26]Comsol Multiphysics, Stockholm, Sweden, "Comsol multiphysics® v. 6.0. www.comsol.com,".

[27]P. Amestoy, I. Duff, and J.-Y. L'Excellent, "Multifrontal parallel distributed symmetric and unsymmetric solvers," Computer Methods in Applied Mechanics and Engineering **184**, 501–520 (2000).

[28]C. Alappat, A. Basermann, A. R. Bishop, H. Fehske, G. Hager, O. Schenk, J. Thies, and G. Wellein, "A recursive algebraic coloring technique for hardware-efficient symmetric sparse matrix-vector multiplication," ACM Trans. Parallel Comput. **7** (2020), 10.1145/3399732.

[29]C. W. Gear, "The numerical integration of ordinary differential equations," Mathematics of Computation **21**, 146–156 (1967).

[30]H. Goldstein, *Classical Mechanics 2nd Ed.* (1980).